PERGAMON

International Journal of Multiphase Flow 25 (1999) 201–228

International Journal of Multiphase Flow

Post-treatment for phase detection probes in non uniform two-phase flows

A. Cartellier

LEG1, Laboratoire des Écoulements Géophysiques et Industriels, UMR 5519 UJF-CNRS-INPG, BP 53, F 38041, Grenoble Cedex 9, France

Received 14 April 1997; received in revised form 1 July 1998

Abstract

The question of the demodulation of raw information delivered by phase detection probes is reconsidered. The standard procedure providing the size distribution from chord measurements is extended along various directions. For spherical inclusions, the presence of flow inhomogeneities is accounted for, both in the case of totally correlated or completely uncorrelated sizes and velocities. Also, the number density, its flux, as well as the mean interfacial area density, become available. Two-phase flow regions close to walls are also considered. It is shown that, using multiple point measurements, the number density flux can be reconstructed with acceptable accuracy. However, the number density and average inclusion velocity relative to centres seem to be out of reach when using only phase detection probes.

Keywords: Phase detection probe; Size distribution; Interfacial area density; Number density; Number density flux; Two-phase (flow)

1. Introduction

Phase detection probes are widely used for the experimental investigation of gas–liquid or liquid–liquid two-phase flows. A simple sensitive tip provides the dispersed phase indicator function X_G. From X_G, the mean inclusion arrival frequency N_d (♯/s) and the local dispersed phase fraction ϵ can be deduced provided that flow conditions are stationary. The velocity of inclusions becomes available using either double or multiple probes (Revankar and Ishii, 1993), or a single tip with an appropriate design (Cartellier, 1992; Pinguet, 1994; Cartellier, et al., 1996; Cartellier, 1997). Usually, only one velocity component w is available. Hence, the latter sensors provide the joint chord (L)—inclusion velocity (w) distribution $\Lambda(L, w)$ (♯/m^2/s), as well as the local dispersed phase volumetric flux j_G. Despite continuous improvements of probe

0301-9322/99/$ - see front matter
PII: S0301-9322(98)00041-X

geometry (Gouirand, 1990; Pinguet, 1994; Cartellier et al., 1996; Cubizolles, 1996; Cartellier, 1997) and of signal processing (Zun et al., 1995, who, in parallel to their own treatment, have also investigated the performance of various more classical techniques; Cartellier, 1997), the above measurements are still subject to limitations mainly induced by the finite size of probes and, sometimes, by incorrect or incomplete signal processing. These problems are not addressed in the following. Instead, this paper focuses on the post-processing, which is intended to extract complementary information from the above-mentioned raw measurements.

The questions which have been addressed thus far, concern the derivation of the size distribution $P(R)$ (Galaup, 1976; Herringe and Davis, 1976) and that of the mean interfacial area density Γ (Galaup, 1976; Katoaka et al., 1986; Hikibi et al., 1997). Both $P(R)$ and Γ are accessible only under strong assumptions about the flow structure (see the review by Cartellier and Achard, 1991). Notably, it is often assumed that the flux of the dispersed phase is locally uniform, and that the size distribution is independent of position. However, most experimental data gathered in confined two-phase flows, demonstrate that phase distribution usually departs from uniformity, and that size segregation is common. In order to improve the experimental description of two-phase flows, our first goal is to relax these assumptions in order to establish more general transformations.

The second objective is connected with the nature of variables to be determined. Indeed, most of the above-mentioned quantities are adapted to the classical two-fluid model, which is based on a continuous description of both phases (Ishii, 1975). Two-phase models using concepts of statistical mechanics and exploiting ensemble averaging (also called kinetics or hybrid approach) are becoming popular (see for example Achard and Cartellier, 1993; Zhang and Prosperetti, 1994; Simonin, 1996). The new quantities introduced to describe the dispersed phase, such as the number density and its flux, are relative to the position of inclusion centres. To ensure proper comparisons between hybrid modelling and experimental results, it is essential to measure these new quantities as directly as possible. However, in order to relate these new unknowns to the usual quantities delivered by probes, namely N_d, j_G ϵ and $\Lambda(L, w)$, one has to account for some bias effects. Indeed, any phase detection probe detects bubbles[1] whose centre is some distance away from the probe tip. Thus, the information available is not relative to bubble centres: instead it is a spatial mean. Besides, the probe being more likely to intercept larger bubbles, probe raw data correspond to a spatial average weighted by the size of inclusions. Many authors have already underlined that the size distribution perceived by a probe differs from the size distribution of the mixture (Galaup, 1976; Herringe and Davis, 1976; Clark and Turton, 1988). Other quantities, such as the number density and its flux are also expected to be sensitive to such effects. Note that quite similar difficulties occur for laser anemometry when applied to large inclusions (see for example Cartellier and Lismonde, 1984; Sommerfeld and Qiu, 1995). However, unlike phase Doppler anemometry, or even imaging techniques, which provide the size of each inclusion, phase detection probes are unable to perceive sizes directly. Consequently, as will be shown in the next sections, the data interpretation requires additional assumptions regarding the flow structure and, ultimately, additional measurements.

[1] In the following, bubbles is often used in place of inclusions.

The paper is organized as follows. In the first section, after introducing the variables associated with the hybrid approach, the information available from an ideal probe is considered and general relationships are established to be used with specific sets of assumptions corresponding to flow structures of practical importance. Sections 2 and 3 are concerned with spatial inhomogeneities of the flow in case of a probe far from walls. Section 4 is devoted to the analysis of measurements performed in the vicinity of walls.

2. Restrictions, hypotheses and general relationships

2.1. Hybrid modelling variables

In the framework of the hybrid approach, the dispersed phase is described by product densities of order of $f^{(1)}$ $(\mathbf{x}, \xi)$ and higher, where $\mathbf{x}$ refers to the position of inclusion centres inside the physical domain D considered, and ξ denotes a set of internal coordinates. ξ includes for example the velocity $\mathbf{V}_0$ of the inclusion mass centre, and some shape and/or size characteristics. In the following, only spherical inclusions are considered, so that ξ is composed of the velocity $\mathbf{V}_0$ and the radius R. The notation $f^{(1)}$ $(\mathbf{x}, \mathbf{V}_0, R)\ \mathrm{d}R\ \mathrm{d}\mathbf{x}\ \mathrm{d}\mathbf{V}_0$ stands for the average number of inclusions with a mass centre velocity within the velocity interval $\mathrm{d}\mathbf{V}_0$ around $\mathbf{V}_0$, with a radius within $[R, R + \mathrm{d}R]$ and a centre in the volume element $\mathrm{d}\mathbf{x}$ around $\mathbf{x}$. Note that $f^{(1)}$ is not a probability density function (pdf), since it is not normalised to one: instead, its integral over the domain described by the parameters $\mathbf{x}$, $\mathbf{V}_0$ and R provides the total number of inclusions present in the flow. The most detailed description provided by the hybrid approach is based on evolution equations for the product densities. It is often more convenient to consider instead moment equations. The most usual moments are:

- the local number density n ($\sharp/\mathrm{m}^3$) obtained by integrating $f^{(1)}$ over all possible radii and velocities:

$$n(\mathbf{x}) = \int \mathrm{d}R \int \mathrm{d}\mathbf{V}_0 f^{(1)}(\mathbf{x}, \mathbf{V}_0, R); \tag{1}$$

- the local average inclusion velocity $\langle \mathbf{V} \rangle$, defined from the local number density flux φ ($\sharp/\mathrm{m}^2/\mathrm{s}$, sometimes called flux of centres) obtained by integrating $\mathbf{V}_0\ f^{(1)}$ over all possible radii and velocities:

$$\varphi(\mathbf{x}) = \int \mathrm{d}R \int \mathrm{d}\mathbf{V}_0 \mathbf{V}_0 f^{(1)}(\mathbf{x}, \mathbf{V}_0, R) = n(x)\langle V \rangle(\mathbf{x}); \tag{2}$$

- the joint position-size product density $P^{(1)}(\mathbf{x}, R)$:

$$P^{(1)}(\mathbf{x}, R) = \int \mathrm{d}\mathbf{V}_0 f^{(1)}(\mathbf{x}, \mathbf{V}_0, R). \tag{3}$$

$P^{(1)}(\mathbf{x}, R)\ \mathrm{d}\mathbf{x}\ \mathrm{d}R$ represents the average number of bubbles of radius between R and $R + \mathrm{d}R$ with centres located in the elementary volume $\mathrm{d}\mathbf{x}$ around $\mathbf{x}$. From (3), one can

define the probability density function for the size conditional upon the presence of centres at $\mathbf{x}$, as:

$$P(R|\mathbf{x}) = P^{(1)}(\mathbf{x}, R)/n(\mathbf{x}). \tag{4}$$

In general, $P(R|\mathbf{x})$ depends on the location $\mathbf{x}$. If sizes are uncorrelated with the position, then $P(R|\mathbf{x})$ reduces to the unconditional size distribution $P(R)$, which is the quantity most often used in the literature. If the size distribution is not independent on position, it is no longer possible to define an unconditional size distribution $P(R)$—except by performing a volume average over the entire domain occupied by the flow, but such information is of limited practical value. Instead, one has to go back to the product density $P^{(1)}(\mathbf{x}, R)$ or to $P(R|\mathbf{x})$, which are unambiguously defined.

To investigate the possibilities offered by phase detection probes to get access to the number density, number density flux, and "size distribution", one has to establish a set of general relations which link the measured parameters N_d, j_G, ϵ and $\Lambda(L, w)$ to the first-order product density function $f^{(1)}$. The analysis is concerned with steady two-phase flows (Restriction $R0$) composed of spherical inclusions (Restriction $R1$). The latter restriction is in agreement with the range of applicability of the kinetics approach itself, which is appropriate for inclusions whose shape can be described by a finite (and preferentially small) number of parameters. It must be mentioned, however, that most of the procedures presented in this paper can be extended to different shapes provided that the internal coordinate ξ is accordingly modified. Yet, as shown by Clark and Turton (1988), analytical expressions are accessible only if all bubbles assume axisymmetric and homothetic shapes (for example, ellipsoidal bubbles with a fixed eccentricity).[2]

Let us consider a probe immersed in a two-phase flow whose tip is located at a point O far from any wall. The z-axis (unit vector $\mathbf{k}$) is directed along the probe axis (Fig. 1), while the plane (Oxy) is normal to $\mathbf{k}$. It is assumed that:

Hypothesis $H0$: the sensor (including its support) is ideal in the sense that its presence does not modify any characteristic of the flow. Notably, it is supposed that all dwell times, velocities and chords are correctly detected and quantified. This latter assumption is clearly not valid in practice, since whatever the sensor considered, there is always a minimum value of the chord under which the probe detects nothing. The actual limit of detection is still not well known (Cartellier and Barrau, 1998a,b).

2.2. General connection between true and detected size distributions

The first step is aimed to relate the true size distribution $P(R)$ at O to the detected size distribution noted P_d. As shown notably by Galaup (1976) and by Herringe and Davis (1976), P_d differs from $P(R)$ because of the evolution of the volume scanned by a probe with the bubble size. Let us start by expressing the average total number of bubbles N_d detected per unit time by the probe at O. To evaluate N_d, one has to sum up the hits due to any bubble size, velocity and position, provided that the bubbles interact with the probe tip located at O.

[2] Solutions are also available when the shape is uniquely connected to the size.

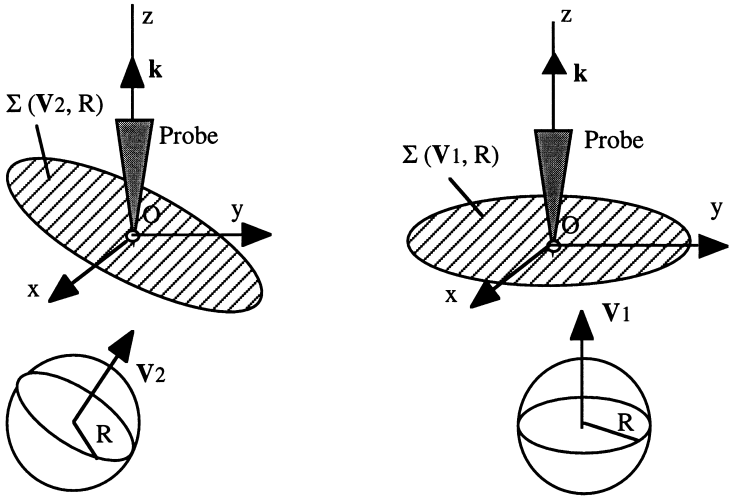

Fig. 1. Sketch of the extent of the probing area Σ for a fixed bubble size and for two velocities.

Thus,

$$N_{\mathrm{d}} = \int \mathrm{d}R \int \mathrm{d}\mathbf{V}_0 \int_{\mathbf{x}\in\Sigma(\mathbf{V}_0,R)} \mathrm{d}\mathbf{x}\, V_0 f^{(1)}(\mathbf{x}, R, V_0), \tag{5}$$

where the spatial integration is performed over the probing area $\Sigma(\mathbf{V}_{\mathrm{o}}, R)$ defined in a plane perpendicular to the velocity and those extend depends on the bubble size (Fig. 1). Since phase detection probes provide a single velocity component, this equation is too general to be exploited. To obtain tractable expressions, the following simplifications are introduced:

- Hypothesis $H2$: $f^{(1)}$ is assumed not to depend on the z coordinate.

A consequence of the hypotheses $H1$ and $H2$ is that, far from walls, the probing area $\Sigma(R)$ is the disc of radius R centred at O. Thus:

$$N_{\mathrm{d}} = \int \mathrm{d}R \int \mathrm{d}w \int_{(x,y)\in\Sigma} \mathrm{d}x\, \mathrm{d}y\, w\, f^{(1)}(x, y, R, w) = \int n_{\mathrm{d}}(R)\, \mathrm{d}R. \tag{6}$$

In [6], the second equality defines the average number n_{d} of detected bubbles of size R per unit time.

To go further, additional simplifications of the function $f^{(1)}$ must be made because, with a single probe, it is difficult to distinguish between the influence of velocity and size on the number of hits. Various sets of assumptions will be introduced in Sections 2–4 depending on the type of flow considered.

2.3. General connection between detected chords and sizes

The second relation required must link the detected chord to the flow characteristics. Starting from the product density $f^{(1)}$ (x, y, z, w, R), it is possible to express a product density

$f^{(1)}(L, y, z, w, R)$, where L is defined as:

$$L = 2\sqrt{R^2 - (x^2 + y^2)}. \tag{7}$$

Indeed, the function $L(x, y)$ given by (7) being continuous and monotone, one can write (Dubes, 1968):

$$f^{(1)}(L, y, z, w, R) = \left|\frac{\partial L}{\partial x}\right|^{-1} f^{(1)}(x, y, z, w, R) = \frac{L}{2x_0} f^{(1)}(x_0, y, z, w, R), \tag{8}$$

where:

$$x_0 = \sqrt{R^2 - (L/2)^2 - y^2}. \tag{9}$$

In the above relations, L represents the chord detected by a probe at O, from a bubble of radius R whose centre crosses the (Oxy) plane at the coordinates (x_0, y) during its movement along z. This new product density is only meaningful for loci (x, y) within a distance R or less from O.

To evaluate the average number of chords of value L detected per unit time from bubbles at a fixed y coordinate, noted $\Lambda^{(1)}(L, y, R)$, the flux of $f^{(1)}(L, y, z, w, R)$ has to be integrated over all velocity realisations. Hence:

$$\Lambda^{(1)}(L, y, R) = \int \mathrm{d}w\, w\, f^{(1)}(L, y, z, w, R), \tag{10}$$

or, using (8), and taking into account the hypothesis $H2$:

$$\Lambda^{(1)}(L, y, R) = \int \mathrm{d}w \frac{L}{2x_0} w\, f^{(1)}(x_0, y, z = 0, w, R). \tag{11}$$

The product density $\Lambda^{(1)}(L, R)$ is the integral of $\Lambda^{(1)}(L, y, R)$ over all possible locations y, such that a chord of value L is detected from a bubble of radius R (Fig. 2). According to (9), and for a probe far from walls, y ranges over the interval [–a, a], where a is the positive root

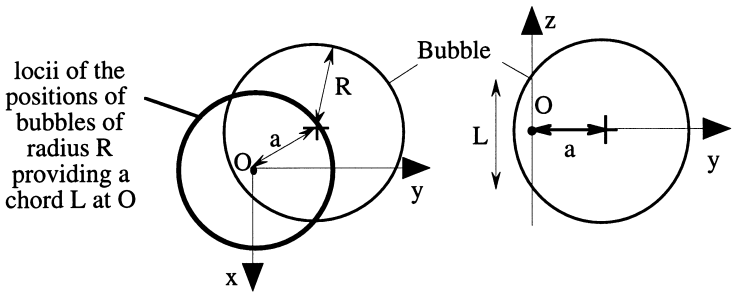

Fig. 2. Chord detection and the position of contributing bubbles for $\mathbf{V}_0 = w\mathbf{k}$.

of $a^2 = R^2 - (L/2)^2$. Thus:

$$\Lambda^{(1)}(L, R) = \int_{-a}^{a} \mathrm{d}y \int \mathrm{d}w \frac{L}{2x_0} w f^{(1)}(x_0, y, z = 0, w, R) \tag{12}$$

The chord product density $\Lambda^{(1)}(L)$ is obtained by integrating $\Lambda^{(1)}(L, R)$ over the various bubbles radii able to produce a chord L. Since only bubbles of radius $L/2$ and greater may contribute to $\Lambda^{(1)}(L)$, the lower limit of integration is $L/2$. The upper limit is the maximum radius present in the flow, denoted $R_{\max}$. Thus:

$$\Lambda^{(1)}(L) = \int_{L/2}^{R_{\max}} \mathrm{d}R \int_{-a}^{a} \mathrm{d}y \int \mathrm{d}w \frac{L}{2x_0} w f^{(1)}(x_0, y, z = 0, w, R), \tag{13}$$

and the detected chord distribution $\Lambda(L)$ equals $\Lambda(L)/N_{\mathrm{d}}$.

Note that in (13), it is possible to account for some defects in detection by introducing the minimum chord C that can be perceived by a given probe. If C does not depend on the inclusion velocity, it is just required to replace the lower boundary in the integral over the radius in (13) by the maximum of C and $L/2$ instead of $L/2$. However, the limit of detection is likely to be expressed as a minimum dwell time, so that the minimum chord C may evolve with the bubble velocity: if so, the exploitation of (13) will become more difficult.

After having established some general transformations, it is now possible to specify the meaning of "a probe far enough from the walls". Indeed, for the above equations to be valid, the probing area $\Sigma(\mathbf{V}_0, R)$ must not be altered by the presence of walls. Hence, due to hypothesis $H2$, it is required that the distance between the probe and any wall is greater than the maximum diameter of the inclusions at the probe location. This constraint applies to Sections 2 and 3, in which spatial variations of the local dispersed phase flux are considered.

3. Non-homogeneous flows with uncorrelated size-velocity distributions

Additional hypotheses are now required, namely:

Hypothesis $H3$: the velocities and sizes are uncorrelated. This seems a reasonable hypothesis for a large class of two-phase flows, because turbulence or particle interactions weaken the correlation between size and velocity. Clearly, the assumption $H3$ could be unrealistic in some situations and a total correlation could be assumed instead. This case is considered in Section 3.

Hypothesis $H4$: the sizes and positions are uncorrelated. This requires that no size segregation occurs: such a hypothesis could be incorrect, for example, in a strong shear field where transverse forces become significant.

Very generally, $f^{(1)}(\mathbf{x}, \mathbf{V}_0, R)$ could be written as the product $g^{(1)}(\mathbf{x}, \mathbf{V}_0|R)\ P(R)$, where $g^{(1)}$ is a product density conditioned by the size R. With hypotheses $H3$ and $H4$, the size conditioning disappears from $g^{(1)}$, and $P(R)$ is exactly the unconditional size distribution mentioned in Section 2.1. Then, from (6), the average number n_{d} of detected bubbles of size R per unit time becomes:

$$n_{\mathrm{d}}(R) = \int \mathrm{d}w \int_{|x^2+y^2|\leq R^2} \mathrm{d}x\, \mathrm{d}y\, w\, g^{(1)}(x, y, w) P(R). \tag{14}$$

To exploit the above equation, one has to specify some characteristics of the function $g^{(1)}$. All the relations available in the literature assume that $g^{(1)}$ is spatially uniform except Galaup (1976), who has tried to account for a dispersed phase fraction gradient. His attempt will be discussed at the end of this Section.

3.1. Relation between true and detected size distributions

Equation (14) accounts for any variation of the dispersed phase velocities and their number density (included in $g^{(1)}$) with the coordinates x and y. To exploit (14), let us consider a flow with strong variations along the y-direction, but no gradient along the x-direction (Fig. 3). This situation is encountered in plane flows, but it is often locally valid for a more general class of two-phase flows. It is thus, assumed that, Hypothesis H5: $f^{(1)}$ does not depend on the x coordinate.

Performing the integration along x in (14) leads to:

$$\begin{aligned} n_{\mathrm{d}} &= P(R) \int \mathrm{d}w \int_{-R}^{+R} \mathrm{d}y \int_{-\sqrt{R^2-y^2}}^{\sqrt{R^2-y^2}} \mathrm{d}x\, w(y)\, g^{(1)}(y, w) \\ &= P(R) \int_{-R}^{+R} \mathrm{d}y\, 2\sqrt{R^2-y^2} \left[\int \mathrm{d}w\, w(y)\, g^{(1)}(y, w) \right]. \end{aligned} \tag{15}$$

The bracketed term in the right-hand side (rhs) of (15) represents the number of bubbles centred at y per unit surface (normal to $\mathbf{k}$) and per unit time. Since R and w are uncoupled, and according to (2), this term is exactly the number density flux $\varphi(y) = n(y)\langle w\rangle(y)$. Thus:

$$n_{\mathrm{d}}(R) = P(R) \int_{-R}^{+R} \mathrm{d}y\, 2\sqrt{R^2-y^2}\, \varphi(y). \tag{16}$$

The integral on the RHS of (16) depends on R and on the spatial distribution of the number density flux in the vicinity of the probe. Let us denote this integral by $B(R, \varphi)$ so that (16)

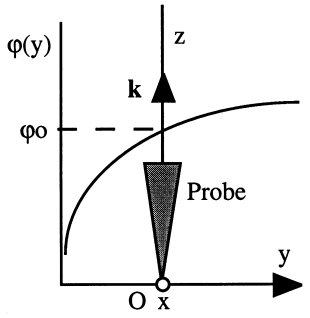

Fig. 3. Number density flux profile in the vicinity of the probe.

reads:

$$n_d(R) = B(R, \varphi)P(R). \tag{17}$$

From the definition of the detected size distribution $P_d(R)$, we have:

$$n_d(R) = N_d P_d(R) \tag{18}$$

The size distribution of detected bubbles $P_d(R)$ can now be connected to the size distribution relative to centres $P(R)$. Eliminating $n_d(R)$ by combining (17) and (18), ones obtains $P(R) = [N_d/B(R, \varphi)]P_d(R)$. Since $P(R)$ is a true pdf, its integral over R equals one, so:

$$N_d = 1/\int dR[P_d(R)/B(R, \varphi)], \tag{19}$$

and

$$P(R) = \frac{P_d(R)}{B(R, \varphi)}\left[\int dR \frac{P_d(R)}{B(R, \varphi)}\right]^{-1}. \tag{20}$$

Formula (20) accounts for the evolution of the probe volume with the size of inclusions: the weighting factor B includes the effect of the radius, as well as that of a spatial variation of the bubble flux along one coordinate.

In order to derive expressions of practical use, let us consider a Taylor expansion of the number density flux valid in the vicinity of the probe position O, i.e. $\varphi(y) = \varphi_0(1 + py + qy^2)$, where $p = \partial(\varphi/\varphi_0)/\partial y|_0$ is the local gradient of the dimensionless number density flux and $q = (1/2)\ \partial^2(\varphi/\varphi_0)/\partial y^2|_0$ is half the local curvature of the dimensionless number density flux. Performing the integral in (16) that defines B, it follows that:

$$B(R, \varphi) = \pi R^2 \varphi_0 (1 + qR^2/4). \tag{21}$$

The total number of detected bubbles per unit time (or the bubble arrival frequency), which equals the integral over R of n_d, is:

$$N_d = \pi\varphi_0\left(\overline{R^2} + \frac{q}{4}\overline{R^4}\right), \tag{22}$$

where $\overline{R^2}$ and $\overline{R^4}$ represent, respectively, the second and fourth moments of the distribution $P(R)$ (and not $P_d(R)$!). Formula (20) becomes:

$$P(R) = \frac{P_d(R)}{R^2(1 + qR^2/4)}\left[\int dR \frac{P_d(R)}{R^2(1 + qR^2/4)}\right]^{-1}. \tag{23}$$

For a spatially uniform flux, $\varphi(y) = \varphi_0$, the weighting factor B equals $\pi R^2\varphi_0$, and (23) reduces to the classical relationship derived many times, notably by Herringe and Davis (1976):

$$P(R) = \frac{P_d(R)}{R^2}\left[\int dR \frac{P_d(R)}{R^2}\right]^{-1}. \tag{24}$$

An important feature of the above results, is that the gradient p is absent from (21) to (23). Indeed, for a flux evolving linearly with one space coordinate, all the flux deficit on one side of the probe (say for $y < 0$), is compensated by the larger contribution from the other side (say $y > 0$), and the final result is identical to that obtained for a uniform number density flux equal to the flux value at the probe position O. However, whenever the curvature $2q$ differs from zero, there is no longer a balance between contributions from each side of the probe, and the transformation between observed and actual size distributions must account for the squared variation of the flux with position, as shown by (23). Also, from (22), the bubble arrival frequency becomes sensitive to the fourth moment of the true size distribution.

According to (23), the experimental determination of $P(R)$ requires the knowledge of the detected distribution $P_d(R)$, as well as that of the curvature of the flux spatial distribution. Let us now consider the determination of $P_d(R)$.

3.2. Link between chord and size distributions

To obtain $P_d(R)$, one must exploit the detected chord distribution $\Lambda(L)$. Using $H3$ and $H4$ to decompose $f^{(1)}$ as $g^{(1)}P(R)$, (13) becomes:

$$\begin{aligned}\Lambda^{(1)}(L) &= \frac{L}{2}\int_{L/2}^{R_{\max}} \mathrm{d}R\ P(R) \int_{-a}^{a} \mathrm{d}y \frac{1}{x_0} \int \mathrm{d}w\ w\ g^{(1)}(x_0, y, z=0, w) \\ &= \frac{L}{2}\int_{L/2}^{R_{\max}} \mathrm{d}R\ P(R) \int_{-a}^{a} \mathrm{d}y \frac{\varphi(x_0, y)}{x_0},\end{aligned} \tag{25}$$

since the integral over the velocity is precisely the number density flux at the coordinate (x_0, y) i.e. $\varphi(x_0, y)$.

Again, to derive a useful formula, the form of the spatial evolution of $\varphi(x_0, y)$ must be specified, and as before, a Taylor expansion is considered. Evaluating the integral over y involved in (25), one finds:

$$\Lambda^{(1)}(L) = \varphi_0 \frac{\pi}{2}\int_{L/2}^{R_{\max}} \mathrm{d}R\ P(R) L\left(1 + q\frac{R^2 - (L/2)^2}{2}\right). \tag{26}$$

The factor inside brackets represents the relative weight of the contribution of bubbles of size R to the chords of value L. Alternately, one can introduce the detected size distribution $P_d(R)$. Using (19)–(21), one obtains:

$$\Lambda^{(1)}(L) = N_d \int_{L/2}^{R_{\max}} \mathrm{d}R\ P_d(R) \frac{L}{2R^2} \frac{\left(1 + q\dfrac{R^2 - (L/2^2)}{2}\right)}{\left(1 + q\dfrac{R^2}{4}\right)}. \tag{27}$$

Assuming a spatially uniform distribution of the flux, q is zero and formula (27) reduces to the usual chord/size relationship (see for example the formula (50) in Cartellier and Achard, 1991). As noted before for the link between true and detected size distributions, the gradient p does

not appear in the derivation due to symmetry, but the curvature q appears explicitly in the chord/size relationship (27).

To invert (27) in practice, it is convenient to use a procedure proposed by Galaup (1976) and by Clark and Turton (1988). If $R_{\max}$ denotes the largest bubble radius, the maximum chord $L_{\max}$ which can be detected, is 2 $R_{\max}$ for spherical inclusions. Chord and radii are then discretized as follows:

$$L_i = i\Delta L \text{ for } i = 0 \ldots 1, \text{ so that } L_{\max} = 1\Delta L;$$
$$R_j = j\Delta R \text{ for } j = 0 \ldots m, \text{ where } R_{\max} = m\Delta R \text{ must not be less than } L_{\max}/2.$$

The integration performed from $L/2$ to $R_{\max}$ in (27), is replaced by a sum over j which begins at $j = k$ such that $2R_k \geq L_i$. Thus:

$$\Lambda(L_i) = \sum_{j=k}^{m} \Delta R \frac{L_i}{2R_j^2} \frac{(1 + q[R_j^2 - L_i^2/4]/2)}{(1 + qR_j^2/4)} P_d(R_j) = \sum_{j=0}^{m} C_{ij} P_d(R_j) \Delta R, \tag{28}$$

and the coefficients C_{ij} are defined by:

$$\begin{aligned} C_{ij} &= \frac{L_i}{R_j^2} \frac{(2 + q[R_j^2 - L_i^2/4])}{(4 + qR_j^2)} \quad \text{for } j \geq k; \\ &= 0 \qquad\qquad\qquad\qquad\quad \text{for } j < k. \end{aligned} \tag{29}$$

The triangularity of (28) allows us to solve for $P_d(R)$, providing q is known. In practice, artefacts can occur because of the sensitivity of the reconstruction to the choice of the discretisation of chords and radii: this question will not be touched upon here.

3.3. Determination of the number density flux and its spatial evolution

In Section 3.1 and 3.2, relationships have been established between the chord distribution, the detected radius distribution and true radius distribution. The next step consists of determining the number density flux φ_0 at the measuring location O. For that, it is convenient to start from the expression of the average bubble arrival frequency N_d. Introducing in (19) the function B given by (21), ones obtains:

$$\varphi_0 = \frac{1}{\pi} N_d \int_0^{R_{\max}} dR \, [P_d(R)/[R^2(1 + qR^2/4)]]. \tag{30}$$

Since φ_0 depends both on $P_d(R)$ and on q, while $P_d(R)$ depends only on q, (30) cannot be solved directly. Instead, the following iterative process is proposed. First, q is set to zero, and initial guesses $P_d^0(R)$ and φ_0^0 can be estimated, respectively, for the detected size distribution from (27), and for the flux from (30). Since additional information is required to evaluate q, the probe is positioned at two new locations, say A and B on both sides of O along the y-direction. Assuming again a uniform number density flux at all positions, initial guesses φ_A^0 and φ_B^0 become available, from which a first estimate of the curvature, denoted as q^1, can be deduced. The same procedure is used again by introducing this curvature q^1 in (27) and (30),

so that a new detected size distribution $P^1_d(R)$, and new number density fluxes φ^1 can be computed at the three probe locations A, O and B. The above process can be repeated until a satisfactory convergence is ensured for φ_0 and q. Since it has not been demonstrated that such a convergence must occur, the validity of the procedure will be checked on an example in Section 3.7. Finally, the true size distribution $P(R)$ can be computed from (23). The above procedure implicitly assumes that the curvature is the same for the three probe positions considered. To eliminate this assumption, the above iterative process has to be applied to a larger set of measuring locations.

An alternate possibility to evaluate the "initial" value of φ_0 has been proposed and used by Cubizolles (1996): it is based on the determination of the slope of the function $\Lambda(L)/L$ for $L \to 0$. For clarity, we include the demonstration here. Starting from (27) divided by N_d, and assuming a uniform flux ($q = 0$), ones obtains:

$$\frac{\Lambda(L)}{L} = \frac{\varphi_0}{N_d}\frac{\pi}{2}\int_{L/2}^{R_{max}} dR\, P(R), \tag{31}$$

which, after differentiating with respect to L, leads to:

$$\frac{d}{dL}\left(\frac{\Lambda(L)}{L}\right) = -\frac{\varphi_0}{N_d}\frac{\pi}{2}P(L/2). \tag{32}$$

Since P is a true probability density function, its integral over all values of the random variable is unity. Applying this to (32) leads to:

$$-\left[\frac{\Lambda(L)}{L}\right]_0^\infty = \frac{\varphi_0}{N_d}\frac{\pi}{2} \approx \frac{d\Lambda}{dL}_{L\to 0}. \tag{33}$$

To successfully apply this direct procedure, it is required that the chord distribution is smooth enough for its slope at the origin to be accurately determined, implying a very large number of realisations. Further, since a probe misses or improperly measures the smallest chords, not to mention the possible validation of some signal noise as bubbles, the chord distribution is expected to be inaccurate for small chord lengths. Hence, the slope must be estimated over a finite chord interval, and deviations from the actual value of $d\Lambda/dL$ at the origin could occur. In practice, according to the above comments, it appears crucial to check precisely the sensitivity of slope measurement. Note also that a relation such as (33) cannot be derived if the flux is not spatially uniform.

3.4. Determination of the number density and its spatial evolution

For the determination of the number density, the local dispersed phase fraction ϵ must be exploited. ϵ can be expressed versus $f^{(1)}$. Indeed, for spherical inclusions, ϵ results from the contributions of all inclusions whose centre is enclosed in a sphere those radius equals that of each inclusion considered. Hence, the void fraction at the origin O is (see Cartellier and Achard, 1991):

$$\epsilon = \int \mathrm{d}R \int \mathrm{d}\mathbf{V}_0 \int_{|\mathbf{x}| \le R} \mathrm{d}\mathbf{x}\, f^{(1)}(\mathbf{x}, \mathbf{V}_0, R). \tag{34}$$

With the help of hypotheses $H2$, $H3$ and $H4$ (note that $H1$ is not required), one obtains:

$$\epsilon = \int P(R)\, \mathrm{d}R \int_{|\mathbf{x}| \le R} \mathrm{d}\mathbf{x} \int \mathrm{d}\mathbf{V}_0 g^{(1)}(\mathbf{x}, \mathbf{V}_0). \tag{35}$$

The integral of $g^{(1)}$ over all velocity realisations is precisely the number density n at the position $\mathbf{x}$. Whatever the velocities of inclusions (in direction and magnitude), the dispersed phase fraction is given by:

$$\epsilon = \int P(R)\, \mathrm{d}R \int_{|x| \le R} \mathrm{d}\mathbf{x}\, n(\mathbf{x}). \tag{36}$$

To proceed further, let us introduce a local Taylor expansion for the number density spatial distribution along the direction y, n being assumed independent of x and z coordinates. Introducing the form $n(y) = n_0 (1 + sy + ty^2)$, where $s = \partial(n/n_0)/\partial y|_O$ is the local gradient of the dimensionless number density and $2t = \partial^2(n/n_0)/\partial y^2|_O$ its local curvature at O, the volume integral in the RHS of (36) can be evaluated, leading to:

$$\epsilon = \frac{4}{3}\pi n_0 [\overline{R^3} + \frac{t}{5}\overline{R^5}]. \tag{37}$$

For a spatially uniform number density, the dispersed phase fraction simply equals the number density times the average volume of the bubbles present in the flow. For reasons of symmetry, the dispersed phase fraction is independent of the local gradient s of the number density. Yet, it depends on its curvature t, weighted by the fifth moment of the true radius distribution $P(R)$.

In uniform flows, n_0 can be deduced from (37) once the size distribution $P(R)$ has been determined. In presence of a curvature, t must be evaluated beforehand. It should be noted that if the spatial distribution of n is not homogeneous, then the number density flux φ evolves also with space coordinates, and the iterative procedure presented in Section 3.3 must be used first to determine q, φ_0 and $P(R)$. Once these variables are known, another iterative process is needed to solve (37) for n_0 and t. Again, an "initial" value n_0^0 for the number density is estimated imposing $t = 0$ in (37). From phase fraction measurements at various positions in the vicinity of point O, a curvature t^1 can be evaluated. Inserting t^1 in (37), a new value n_0^1 can be deduced, and the process can be repeated until convergence. As before, additional measuring locations could be used to more precisely describe the profile of the number density.

3.5. Flow chart of the post-treatment

At this point, all the required variables have been extracted from the raw measurements. The possibilities offered by the post treatment are summarised in Fig. 4. Let us recall the various restrictions and hypothesis required: ideal sensor ($H0$) at a distance to any wall greater than the maximum bubble diameter at this location; steady ($R0$) and fully developed ($H2$: $f(1)$ independent on z coordinate) two-phase flow ($R0$) with spherical inclusions (R1) travelling along the z-direction ($H1$); spatial variations along a single direction y in a plane perpendicular

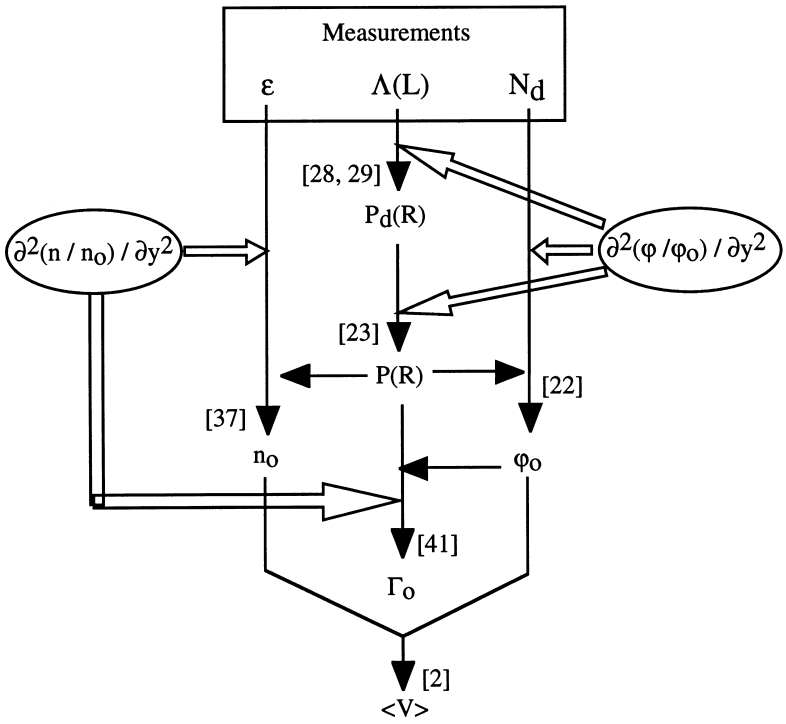

Fig. 4. Chart for the exploitation of raw data under assumptions *H*0–*H*5.

to the *z*-axis (*H*5), with smooth variations so that local Taylor expansions are valid for the number density and its flux; no seggregation effect (*H*4 position and bubble size distribution are decorrelated) and no correlation between bubble size and velocity (*H*3). Such conditions could be approximately satisfied in turbulent bubbly flows with a strong imposed pressure gradient.

The upper box in Fig. 4 represents the raw information available from an ideal probe. It should be noted that the dispersed phase volumetric flux j_G does not appear in this list, although it is accessible to phase detection probes. This is because it does not add any information, as shown by the following equalities:

$$j_G = \frac{\sum_i T_{Gi} w_i}{\Delta t} = \frac{\sum_i L_i}{\Delta t} = \int_0^{2\,R_{max}} L\Lambda^{(1)}(L)\,dL = N_d \int_0^{2\,R_{max}} L\Lambda(L)\,dL, \tag{38}$$

where i indexes the bubbles detected during Δt, and where T_{Gi}, w_i and L_i are, respectively, the dwell time, the velocity and the chord of the ith bubble.

As shown by Fig. 4, starting with the void fraction ϵ, the mean arrival bubble frequency N_d and the chord distribution $\Lambda(L)$, one can deduce the true size distribution $P(R)$, the number density flux φ_0 and the number density n_0 at the measuring location providing that the variables φ_0 and n_0 evolve linearly with space coordinates x and/or y: these derivations are indicated by thin arrows. Whenever the spatial evolutions of the variables φ_0 and n_0 have local curvatures $\partial^2(\varphi/\varphi_0)/\partial y^2\big|_O$ and $\partial^2(n/n_0)/\partial y^2\big|_O$, multiple point measurements must be considered to perform the required transformations. These constraints are indicated by thick arrows in

Fig. 4. Note that, since the size distribution is not a function of space (see hypothesis $H4$), it is equivalent checking the spatial distribution of ϵ instead of n because of (37). Similarly, j_G can be considered instead of φ, because, combining (26) and (38), one obtains:[3]

$$j_G = \varphi_0 \frac{\pi}{2} \int_0^{R_{max}} dR \int_0^{2R} dL\ P(R) L^2 \left(1 + q \frac{R^2 - (L/2)^2}{2}\right) = \frac{4}{3}\pi\varphi_0 [\overline{R^3} + \frac{q}{5}\overline{R^5}] \tag{39}$$

From φ_0 and n_0, one can deduce the average velocity of bubble centres using (2), paralleling here the estimate of an average dispersed phase velocity in the framework of the classical two-fluid model as equal to j_G/ϵ.

Lastly, the mean interfacial area density at the probe position O remains to be determined. Starting from its general expression for spherical bubbles (see equation (36) in Cartellier and Achard, 1991), then:

$$\begin{aligned} \Gamma_0 &= \int d\mathbf{V}_0 \int dR \int_{|\mathbf{x}| \le R} d\mathbf{x}\ f^{(1)}(\mathbf{x}, \mathbf{V}_0, R)\ \delta(|\mathbf{x}| - R) \\ &= \int P(R)\, dR \int_{|\mathbf{x}| \le R} d\mathbf{x}\ n(\mathbf{x}) \delta(|\mathbf{x}| - R), \end{aligned} \tag{40}$$

where the second equality holds because of the assumptions $H3$ and $H4$ ($H1$ and $H2$ are useless). Owing to the Dirac function, the space integral in the RHS of (40) reduces to an integral over the surface of the sphere centred at O and of radius R. With a number density $n(y)$ in a quadratic form versus y and independent of z and x, elementary computations lead to:

$$\Gamma_0 = 4\pi\, n_0 [\overline{R^2} + \frac{t}{3}\overline{R^4}]. \tag{41}$$

In agreement with the arguments of symmetry already given, both j_G and Γ_0 are independent of the gradient of the number density flux and that of the number density, respectively, but are sensitive to the curvature of these quantities.

It is worthwhile to compare the above findings with the results of Galaup (1976), who has considered the influence of a dispersed phase fraction gradient on the relation between chord and size distributions. His investigation was restricted to an axisymetric spatial distribution of ϵ around the probe, and the result of practical value he proposed is strictly valid on the axis of a cylindrical duct. The most important drawback of his analysis is the assumption that the probability of occurrence of a bubble centre at a given position is proportional to the local phase dispersed fraction: as shown by (25), this probability is controlled by the number density flux and not by ϵ. Hence, since ϵ is connected with the number density, the proposal of Galaup

[3] These equalities can be derived as well from the general relation between the local gas flux and the product density function which writes:

$$j_G = \int dR \int d\mathbf{V}_0 \int_{|\mathbf{x}| \le R} d\mathbf{x}\mathbf{V}_0 f^{(1)}(\mathbf{x}, \mathbf{V}_0, R).$$

is valid provided that the average velocity $\langle \mathbf{V} \rangle = \varphi/n$ is spatially uniform: this is a much stronger limitation that ours.

3.6. Influence of the curvature

For practical purposes, it is interesting to analyse how far the curvature of the number density flux modifies the evaluation of the size distribution. From (27), it seems justified to exploit the data as if the number density flux is locally uniform provided that $q = (1/2)\partial^2(\varphi/\varphi_0)/\partial y^2$ is much less than $2/R_{\max}^2$. To confirm this trend, a reconstruction has been simulated, starting from a true size distribution $P(R)$ in the form of a Gaussian distribution with a mean radius of 1.5 mm and a standard deviation of 0.2 mm. Using the equations presented above, it is straightforward to compute $P_d(R)$ and $\Lambda(L)$ for any given curvature q. In a second step, the true size distribution $P1(R)$ is reconstructed from $\Lambda(L)$ assuming q is zero. The discrepancy between P and $P1$, which measures the influence of curvature, is illustrated in Fig. 5, where q is expressed in mm^{-2}. The distortion is quite small at $q = 0.1$, and becomes significant at $q = 0.5$, which is the limit $2/R_{\max}^2$. For q higher than $1\,\mathrm{mm}^{-2}$, not only the size distribution broadens, but its maximum is shifted toward smaller radii, inducing a large error. It should be mentioned that such curvatures are huge: they correspond to a flux varying in a ratio of at least 5 to 1 between positions 2 mm apart.

It has been also verified that the reconstruction is indeed very accurate when the exact value of q is taken into account. This result holds whatever the magnitude of q.

3.7. Validity of the iterative process

In order to provide a practical mean for the determination of the number density flux, it is worthwhile to check the feasibility and the sensitivity of the iterative procedure proposed in

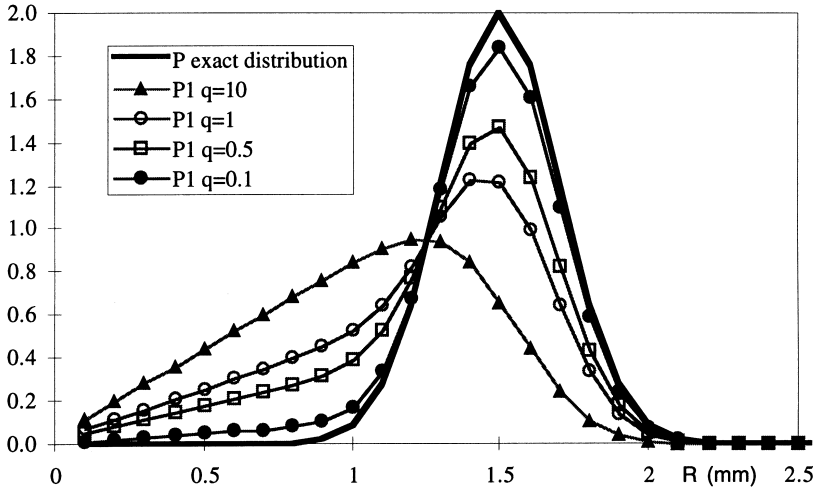

Fig. 5. Influence of the number density flux spatial curvature $2q$ on the reconstructed size distribution $P1$ without correction for q.

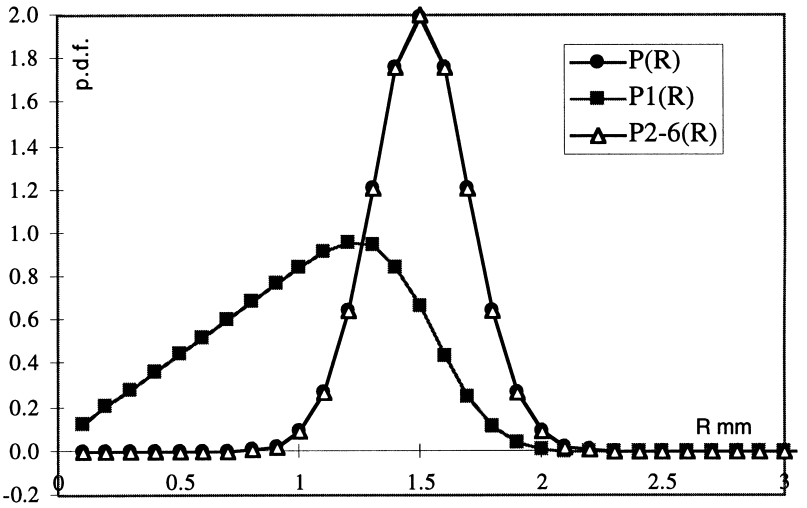

Fig. 6. Result of the iterative process used to reconstruct the size distribution in inhomogeneous conditions ($\varphi_0 = 1\sharp/\mathrm{s/mm^2}$, $p = 1\ \mathrm{mm}^{-1}$, $q = 10\ \mathrm{mm}^{-2}$).

Section 3.3. In that regard, the same size distribution $P(R)$ as in Section 3.6 is considered. Arbitrary values are given for the flux at O, for p and for q. The chosen additional positions A and B are 2 mm away from O. For the particular case $\varphi_0 = 1\sharp/\mathrm{s\ mm^2}$, $p = 1\ \mathrm{mm}^{-1}$ and $q = 10\ \mathrm{mm}^{-2}$, the successive size distributions evaluated during the iteration process are presented in Fig. 6. For the first iteration, which corresponds to computations with $q = 0$, the size distribution $P1(R)$ is incorrect as expected from Section 3.6. However, as soon as the second iteration, the size distribution $P2(R)$ becomes very close to its actual value, and it is almost unaltered for any additional iteration. Fig. 7 illustrates the convergence of other variables: the relative error compared with the actual value is plotted for the flux, its spatial gradient p, spatial curvature q, mean size, and for the fourth moment of the size distribution. For the first step, the error exceeds 1000% for φ_0, it is about −30% on the mean radius, and

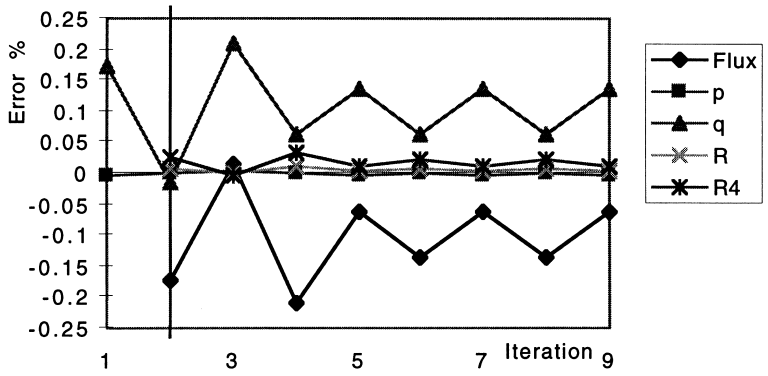

Fig. 7. Convergence of the flux, its gradient p, its curvature q and two moments of the reconstructed size distribution with the number of iterations.

about −60% on the fourth moment of the size distribution. Convergence is almost ensured as soon as the second iteration. After 3–4 iterations, the reconstructed quantities start to oscillate regularly within ±0.2% of their actual values, and no additional progress can be expected. The above trends are observed whatever the values chosen for φ_0, p or q. Therefore, the proposed reconstruction process is valid, and could be used in practice.

4. Non-homogeneous flow with size-velocity correlation

To complement the analysis presented in Section 3, hypotheses $H0$–$H2$ and $H5$ are retained, but hypothesis $H3$ is now replaced by:

Hypothesis$H6$: the velocities and the sizes are totally correlated.

It is not possible to obtain expressions in closed form while maintaining a spatial variation of the local number density flux, and so, $H4$ is replaced by:

Hypothesis $H7$: velocity and size are not correlated with the position. This requires that no size segregation occurs and that the velocity for the dispersed phase is spatially uniform. However, the number density itself can evolve freely around the probe.

According to $H6$ and $H7$, $f^{(1)}$ ($\mathbf{x}$, $\mathbf{V}_0$, R) can be written as the product of the number density $n(\mathbf{x})$ by the size-velocity joint distribution $P(\mathbf{V}_0, R)$. It is then possible to follow the same developments as those presented in the previous sections but considering now $P(\mathbf{V}_0, R)$ instead of $P(R)$.

4.1. Relation between true and detected size-velocity joint distributions

The average number $n_d(R, w)$ of detected bubbles of size R and velocity w is then:

$$n_d(R, w) = \int_{|x^2+y^2|\le R^2} \mathrm{d}x\ \mathrm{d}y\ w\ n(x, y)P(R, w) = w\ P(R, w)\ B(R, n), \tag{42}$$

where the factor B depends on the size R, and on the number density distribution in the vicinity of the measuring location O. As before, n_d is connected, by its definition, to the detected size-velocity joint distribution $P_d(R, w)$:

$$n_d(R, w) = N_d\ P_d(R, w). \tag{43}$$

Combining (42) and (43) provides the required relations:

$$N_d^{-1} = \int_0^\infty \mathrm{d}w \int_0^\infty \mathrm{d}R \frac{P_d(R, w)}{wB(R, n)}, \tag{44}$$

$$P(R, w) = \frac{P_d(R, w)}{wB(R, n)} \left[\int_0^\infty \mathrm{d}w \int_0^\infty \mathrm{d}R \frac{P_d(R, w)}{wB(R, n)} \right]^{-1}. \tag{45}$$

Formula (45) accounts for the evolution of the probe volume with the size of inclusions: the weighting, the radius, as well as that of a spatial variation of the bubble number density along one coordinate. Introducing a Taylor expansion for the one-dimensional spatial evolution of n

and $n(y) = n_0(1 + sy + ty^2)$, one obtains:

$$B(R, n) = \pi R^2 n_0 (1 + tR^2/4). \tag{46}$$

The bubble arrival frequency, which equals the integral over R and w of n_d, is:

$$N_d = \pi\, n_0 (\overline{wR^2} + \frac{t}{4}\overline{wR^4}), \tag{47}$$

where $\overline{wR^2}$ and $\overline{wR^4}$ are moments obtained from the distribution $P(R, w)$ (and not from $P_d(R, w)$!).

4.2. Link between chord and joint size-velocity distributions

Starting from (13), the chord-velocity joint distributions are now expressed as:

$$\Lambda^{(1)}(L, w) = \int_{L/2}^{R_{\max}} \frac{wL}{2} P(w, R)\, \mathrm{d}R \int_{-a}^{a} \mathrm{d}y \frac{n(x_0, y, z = 0)}{x_0}. \tag{48}$$

Introducing the same spatial evolution of n leads to:

$$\Lambda^{(1)}(L, w) = n_0 \frac{\pi}{2} \int_{L/2}^{R_{\max}} \mathrm{d}R\; w\; L\; P(w, R) \left[1 + t\frac{R^2 - (L/2)^2}{2}\right]. \tag{49}$$

This equation is similar to (26), except that the number density n_0 and its curvature t inters the expression instead of the flux and its curvature q, and that the velocity weights the joint chord-velocity distribution. Alternately, $P(R, w)$ could be replaced by $P_d(R, w)$, so that:

$$\Lambda^{(1)}(L, w) = N_d\; w\; L \int_{L/2}^{R_{\max}} \mathrm{d}R \frac{P_d(w, R)}{2R^2} \frac{\left[1 + t\dfrac{R^2 - (L/2)^2}{2}\right]}{\left[1 + t\dfrac{R^2}{4}\right]}. \tag{50}$$

It is then possible to deduce the detected size-velocity joint distribution $P_d(R, w)$ by inverting the above equation, since $\Lambda(L, w) = \Lambda^{(1)}(L, w)/N_d$ is a measured quantity. The inversion technique mentioned at the end of Section 3.2 remains valid: it is only required to apply it for every value of a discrete set of velocities covering the whole interval of variation detected. This process is direct if the local number density is linearly increasing with space coordinates. If a spatial curvature exists, then an iterative process similar to that described in Section 3.3 and involving measurements at various positions in the neighbourhood of O, is required to determine both $P(w, R)$ and t.

4.3. Determination of the number density and its flux

The situation is now slightly different from that investigated in Section 3. Indeed, it is the number density and not its flux which enters in all the above relationships. Once $P(w, R)$ and t are known, n_0 can be deduced from the average bubble arrival frequency N_d using (47). Then,

elementary computations lead to the expressions of the local gas fraction:

$$\epsilon = \frac{4}{3}\pi n_0[\overline{R^3} + \frac{t}{5}\overline{R^5}] \tag{51}$$

and the local gas flux:

$$j_G = \frac{4}{3}\pi n_o\left[\overline{wR^3} + \frac{t}{5}\overline{wR^5}\right]. \tag{52}$$

Note that the curvature t can be estimated equivalently either from (51) or from (52), since the various moments in (51) and (52) are not functions of position due to $H7$. The number density flux is deduced from its definition:

$$\varphi_0 = n_0\bar{w}, \tag{53}$$

where $\overline{w}$ is the average inclusion velocity (averaged over all sizes), deduced from $P(w, R)$. Compared with Section 3, there is no need to introduce the spatial distribution of the number density flux, since according to $H7$, it follows the same law as the number density. Lastly, the average interfacial area density can be deduced from (41), which is still valid. The corresponding flow chart is presented in Fig. 8. It is valid under the following restrictions and hypothesis: ideal sensor ($H0$) at a distance to any wall greater than the maximum bubble diameter at this location; steady ($R0$) and fully developed ($H2$: $f(1)$ independent on z coordinate) two-phase flow ($R0$) with spherical inclusions ($R1$) travelling along the z-direction ($H1$); spatial variations along a single direction y in a plane perpendicular to the z axis ($H5$), with smooth variations so that local Taylor expansions are valid for the number density and its

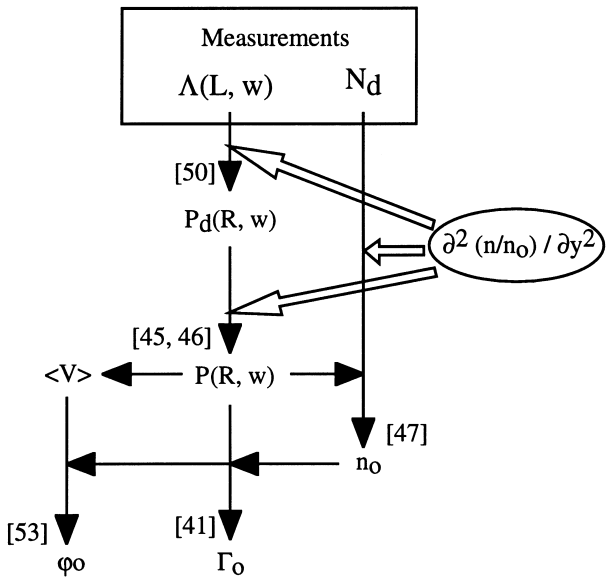

Fig. 8. Chart for the exploitation of raw data under hypotheses $H0$–$H2$ and $H5$–$H7$.

flux; bubble size and velocity are totally correlated (*H*6), but are decorrelated with position (*H*7). Such conditions could be approximately satisfied in creaming bubbly flows or bubbly columns with a weak liquid flow rate.

5. The problem of near-wall zones

Since the wall region is often of great importance when analysing two-phase flows, it is worthwhile to be able to determine the number density and its flux in such zones. This problem, is, however, more complex than those investigated in Sections 3 and 4. Indeed, let us consider a probe tip located at a distance e from a plane wall along the y-direction (Fig. 9). In this section, for convenience, a new system of coordinates is introduced whose origin is at the wall. Restrictions *R*0 and R1 are still valid, as well as hypotheses H0–*H*3. Clearly, it is necessary to account for variations of the two-phase parameters along the direction y normal to the wall, but assumption *H*5 is retained. Besides, the bias effect now obeys a different scaling since, for a distance e less than the maximum inclusion diameter present in the flow, the probing area $\Sigma(w, R)$ is no longer the same as that used in Sections 3 and 4. As bubble centres cannot be located outside the fluid region, $\Sigma(w, R)$ becomes now a function of the probe position e. Moreover, this area is restricted by the interaction of bubbles with the wall. To account for such an effect, and in agreement with restriction R1, it is supposed that no bubble deformation occurs due to the vicinity of walls, so that:

Hypothesis *H*8: the maximum lateral positions of bubbles correspond to their interface touching the wall (Fig. 9). In other words, $f^{(1)}(\mathbf{x}, \mathbf{V}_0, R)$ is zero whenever $\mathbf{x}$ is within a distance R of any wall. This assumption appears to be quite restrictive. However, as far as bubbles remain spherical, wall repulsion forces appear to be strong enough to avoid any contact between bubbles and walls. This is demonstrated by the existence of a near-wall single-phase

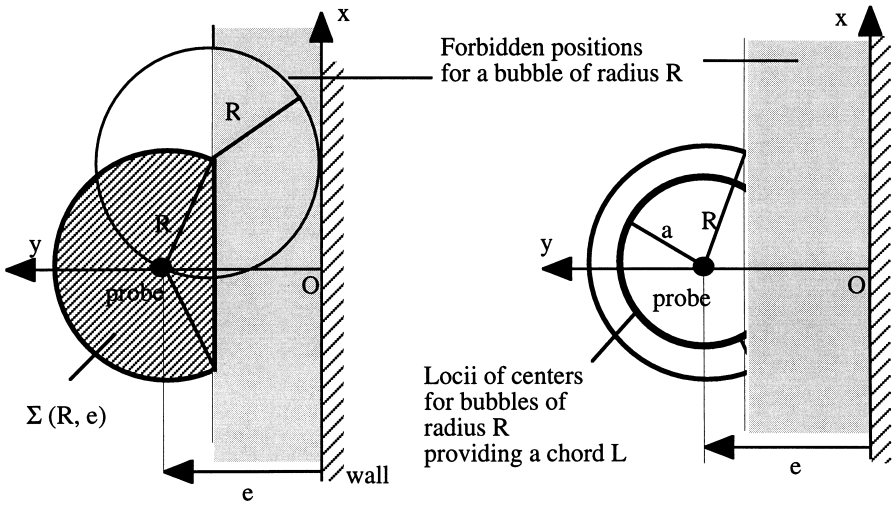

Fig. 9. Sketch of the probing area Σ and the locii of bubble centers contributing to a chord L for a probe in the vicinity of a wall (the z coordinate is normal to the plane of the figure).

layer observed in Poiseuille bubbly flows (Cartellier et al., 1993). This seems to occur also in turbulent conditions although the clear fluid layer is much thinner in that case (Marié, private communication, 1997).

In agreement with $H8$, sizes and positions become correlated, and, since the variations of the velocity with y must also be considered, it is no longer possible to decompose $f^{(1)}(\mathbf{x}, \mathbf{V}_0, R)$ as in Section 3 or 4. A new treatment is thus required.

5.1. Determination of the number density flux

Let us start with the chord distribution perceived by the probe at e, by using (11) which can be rewritten:

$$\Lambda^{(1)}(e, L, y, R) = \frac{L}{2x_0}\varphi(x_0, y, R), \tag{54}$$

where

$$x_0 = \sqrt{a^2 - (y-e)^2};\ a^2 = R^2 - L^2/4. \tag{55}$$

The probing area $\Sigma(R, e)$ is now the portion of the disc of radius R located in the half-plane $y > R$ (Fig. 9). From the definition of $\Sigma(R, e)$, y must pertain to the interval [maz(R, $e-a$), $e+a$], otherwise no chord of value L is detected. Thus, the average number of chords of value L detected at e from bubbles of radius R becomes:

$$\Lambda^{(1)}(e, L, R) = \int_{\max(R, e-a)}^{e+a} \mathrm{d}y \frac{L}{2x_0}\varphi(x_0, y, R), \tag{56}$$

and, using the assumption $H5$, the product density for chords is expressed as:

$$\Lambda^{(1)}(e, L) = N_\mathrm{d}\Lambda(e, L) = \frac{L}{2}\int_{L/2}^{R_\mathrm{max}} \mathrm{d}R \int_{\max(R, e-a)}^{e+a} \mathrm{d}y \frac{\varphi(y, R)}{x_0}. \tag{57}$$

The problem is now to solve the above equation for $\varphi(y, R)$. Clearly, this cannot be accomplished using the information collected from a single position of the probe. One has to consider instead a set of measurements obtained by varying the distance to the wall. To derive equations helpful in practice, the form of the evolution of the flux along the y coordinate must again be specified. Owing to the structure of (57), an expression for $\varphi(y, R)$ is now required instead of $\varphi(y)$. In the vicinity of any position e, the following expansion is assumed to be valid:

$$\varphi(y, R) = \varphi_0(e, R)\,[1 + p(e, R)(y-e) + q(e, R)(y-e)^2]. \tag{58}$$

Introducing the above expression in (57), the joint chord-radius product density becomes:

$$\Lambda^{(1)}(e, L, R) = \frac{L}{2}\varphi_0(e, R)\,[C_0(e, R, L) + p(e, R)C_1(e, R, L) + q(e, R)C_2(e, R, L)], \tag{59}$$

where the functions C_0, C_1 and C_2 obey:

For $e \leq R-a$: $C_0 = C_1 = C_2 = 0$

For $R-a < e < R+a$: C_0, C_1 and C_2 are given by:

$$C_0(e, L, R) = \frac{\pi}{2} - a \sin\frac{R-e}{a},$$

$$C_1(e, L, R) = -a\sqrt{1-\left(\frac{R-e}{a}\right)^2}, \tag{60}$$

$$C_2(e, L, R) = \frac{a^2}{2}C_0 + \frac{R-e}{2}C_1.$$

For $e \geq R+a$: $C_0 = \pi$, $C_1 = 0$, $C_2 = \pi a^2/2$.

The product density for the chords $\Lambda^{(1)}(e, L)$ perceived at e is thus given by:

$$\Lambda^{(1)}(e, L) = \frac{L}{2}\int_{L/2}^{R_{\max}} \mathrm{d}R\ \varphi_0\ [C_0(e, R, L) + p(e, R)C_1(e, R, L) + q(e, R)C_2(e, R, L)]. \tag{61}$$

For probe positions larger than $2R_{\max}$, (61) reduces as expected to the case treated in Section 3. For a probe close to the wall, the first weighting factor C_0, which evolves between 0 and π, affects the number density flux at the measuring location. A second effect, quantified by C_1, is connected with the gradient of the flux: the symmetry responsible for the disappearance of this term in Sections 3 and 4 no longer exists, due to the nearby wall. Last, a third correcting factor C_2 affects the curvature of the flux.

To solve (61) for $\varphi(e, R)$, an iterative procedure similar to that presented in Section 3 could be imagined. For measurements collected at various distances e, the first iteration is performed assuming that $p(e, R)$ and $q(e, R)$ are zero for all values of e and R. Then estimates $p^1(e, R)$ and $q^1(e, R)$ can be deduced at each location e using the flux φ^0 evaluated at neighbouring positions. Using p^1 and q^1 in (61), new values φ^1 for the local flux are produced. The process has to be repeated until convergence. However, it is worthwhile to check the feasibility of this iterative procedure, because, due to the strongly varying weighting functions in (61), it is not clear whether convergence can be ensured. Notably, due to the range of variation of C_0, numerical errors are expected at least very close to the wall where C_0 drops to zero. To diminish such an effect, it could be advantageous to extend the measuring positions up to $2R_{\max}$ or even further from the wall, in order to dispose of some accurate estimates of the fluid and its gradient and curvature. This comment is supported by the fact that, far from walls, the inversion performed using (61) is nearly as accurate as the inversion presented in Section 3.

To test the iterative process, we choose to treat an artificial case. As sketched in Fig. 9, the wall corresponds to the Oxy plane. Far from the wall, the size distribution is Gaussian. Bubbles of all classes are allowed to touch the plane wall while remaining spherical, and the flux of centres varies with the distance to the wall y, according to a second-order polynomial law. The flux has the following form:

$$\varphi(y, R) = P(R)\ H(y-R)\ \varphi_0\ [1 + \varphi_1 y + \varphi_2 y^2], \tag{62}$$

where $P(R)$ is a Gaussian distribution, H is the Heaviside step function, which is equal to zero when its argument is negative and is equal to one otherwise. φ_0, φ_1 and φ_2 are constants. For the test, the mean radius has been set to 0.15 mm, the standard deviation is 0.02 mm, and we used $\varphi_0 = 1\sharp/\mathrm{mm}^2$ s, $\varphi_1 = 5\,\mathrm{mm}^{-1}$ and $\varphi_2 = 10\,\mathrm{mm}^{-2}$. From (62), the local flux expansions of the form (58) are deduced for a discrete set of positions $\{e_i;\ i = 1,\ \ldots,\ N\}$, and the product densities $\Lambda^{(1)}(e_i,\ L)$ which would be perceived by an ideal probe, are computed according to (61). In practice, the positions e_i considered, vary from 0.1 to 0.6 mm with a 0.1 mm step.

For the reconstruction process, one starts with the knowledge of the product densities $\Lambda^{(1)}(e_i,\ L)$ over the same set of positions $\{e_i;\ i = 1,\ \ldots,\ N\}$. A discretisation of sizes R_j; $j = 1,\ \ldots,\ M$ valid for all positions is introduced. At each position e_i, local expansions of the form (58) are written, the values of $\varphi_0(e_i,\ R_j)$, $p(e_i,\ R_j)$ and $q(e_i,\ R_j)$ being the unknowns. These unknowns obey the set of equations of the form (61) written at all positions: this set is solved using the triangularity of (61) with respect to the chord, and the iterative procedure. The results are given in Fig. 10 as the flux φ versus the radius R for the different distances e_i to the wall. The case $e = 0.6$ mm corresponds to a probe beyond the $2R_{\max}$ limit: the reconstruction is, here, quite satisfactory. The same conclusion holds for positions closer to the wall, where the screening effect of the wall becomes effective. It can be noticed that, down to $e = 0.3$ mm, the various iterations lead to very similar results. This behaviour is probably due to the strong influence of the weighting factor C_0 compared with the contributions associated with the slope and curvature (even if large values have been chosen for these quantities). Much closer to the wall, i.e. for e about 0.2 mm, the second iteration brings, indeed, a noticeable improvement compared with the first, but an 8% discrepancy remains in the maximum value of the flux. For $e = 0.1$ mm, where fluxes are much weaker, the iterative process is clearly necessary to predict the correct flux. Again, a significant discrepancy occurs, which is possibly connected to the abrupt increase of the flux in the vicinity of $R = e$. The deviation from theexact solution does not disappear as the number of iterations increases, since oscillations start to occur. It should be noted that better results are obtained when using a refined discretisation of sizes.

Hence, the proposed iterative scheme seems able to provide the number density fluxes in the vicinity of walls. However, it is difficult to estimate to which extend this technique is accurate, notably because the imposed profile we used (see (62)) is rather smooth. Additional tests are required for more complex profiles.

5.2. The problem of the number density

The number density can, in principle, be determined from the measurements of local void fractions. Using the general expression (34), and introducing the number density $n(\mathbf{x}, R)$ for the size R, one obtains:

$$\epsilon(e) = \int \mathrm{d}R \int_{\mathbf{x}\in B} \mathrm{d}\mathbf{x}(\mathbf{x}, R), \tag{63}$$

where the domain of integration B is the sphere centred at e of radius R minus the portion of this sphere at a distance to the wall less than R. The latter restriction is linked with a number

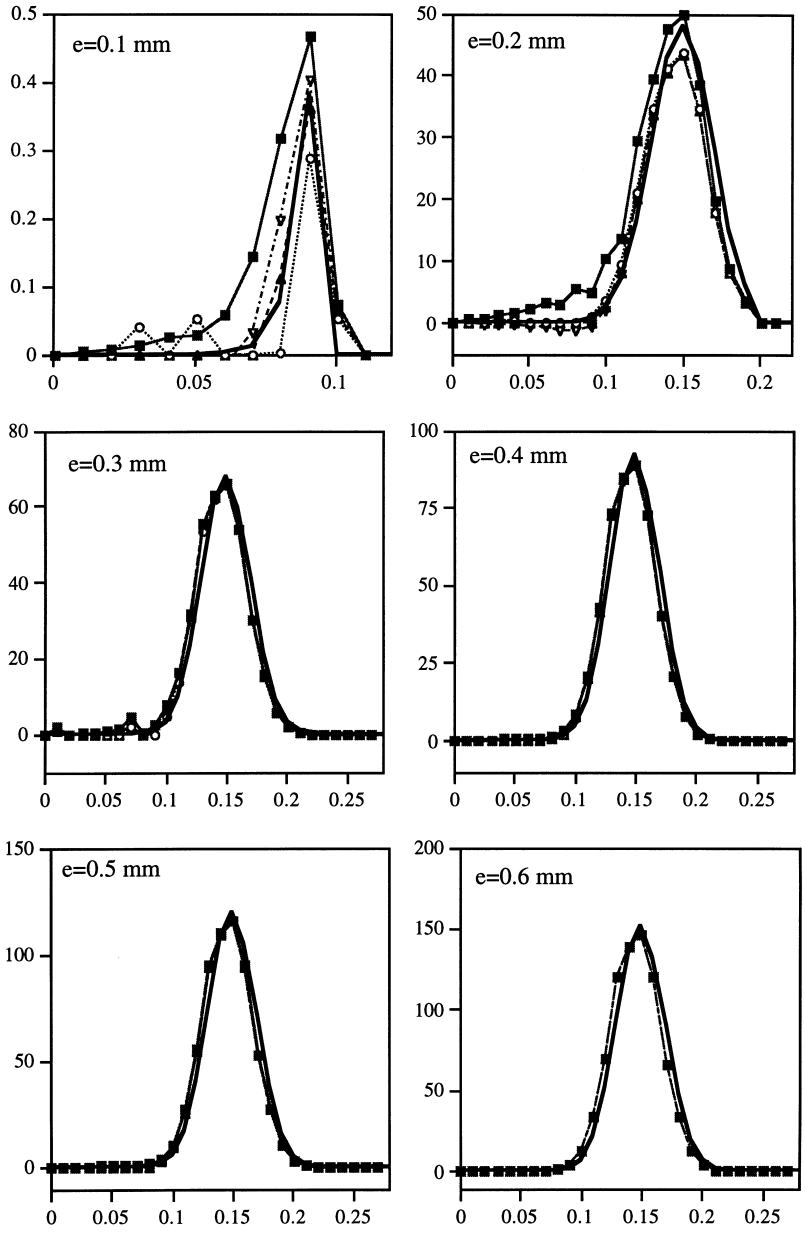

Fig. 10. Plot of the flux versus the radius (in mm) for various positions. (black line = exact solution, squares = first iteration dots = second iteration, closed triangles = third iteration open triangles = fourth iteration).

density which drops to zero whenever y is less than R, in agreement with hypothesis $H8$. As for the flux, it is necessary to account for the spatial evolution of $n(\mathbf{x}, R)$ with the y coordinate, and the following approximation valid in the vicinity of e is considered:

$$n(y, R) = n_0(e, R)\,[1 + s(e, R)(y - e) + t(e, R)(y - e)^2]. \tag{64}$$

Performing the spatial integration in (63) leads to:

$$\epsilon(e, R) = \pi n_0 \left[R^2(R - Z) + s\frac{R^2}{2}(R^2 - Z^2) + \frac{tR^2 - 1}{3}(R^3 - Z^3) - \frac{s}{4}(R^4 - Z^4) - \frac{t}{5}(R^5 - Z^5) \right], \tag{65}$$

where $Z = \max(R - e, -R)$. Since Z equals $-R$ when R is less than $e/2$, and Z is $R - e$ for R higher than $e/2$, the integral over the radius can be split in two contributions, leading to:

$$\epsilon(e)/\pi = \int_{e/2}^{R_{\max}} \mathrm{d}R\; n_0 \left[R^2 e + s\frac{R^2 e}{2}(2R - e) + \frac{tR^2 - 1}{3}(R^3 - Z^3) - \frac{s}{4}(R^4 - Z^4) - \frac{t}{5}(R^5 - Z^5) \right] + \frac{4}{3}\int_0^{e/2} \mathrm{d}R\; n_0 \left[R^3 - t\frac{R^2}{5} \right], \tag{66}$$

and, as expected, (66) leads to (37) when the position e exceeds $2R_{\max}$. In the vicinity of walls, we do not foresee any means to solve (66) for $n_0(e, R)$, $s(e, R)$ and $t(e, R)$, even if measurements of the dispersed phase fraction are available at multiple locations e. The mean interfacial area density is also out of reach since, according to (40) and the extent of B, Γ obeys:

$$\Gamma(e) = 2\pi e \int_{e/2}^{R_{\max}} \mathrm{d}R\; R\; n_0 \left[1 + \frac{s}{2}(2R - e) + \frac{t}{3}\{3R(R - e) + e^2\} \right] + 4\pi \int_0^{e/2} \mathrm{d}R\; n_0 R^2 \left[1 + \frac{t}{3}R^2 \right]. \tag{67}$$

Additional data, issued from alternate measuring techniques or possibly from an improved phase detection technique, seem to be required to fully describe the dispersed phase organisation in the vicinity of walls. For example, Doppler anemometry can give access to the average bubble velocity relative to centres, so that the number density can be determined from $\varphi(e, R)$ using (2).

6. Conclusion

By revisiting the exploitation of raw information issued from phase detection probes in the framework of hybrid (or kinetic) modelling, it has been shown that variables relative to inclusion centres, such as the number density, its flux and the average inclusion velocity, are indeed accessible with such sensors. For a probe located away from walls by an amount at least twice the maximum bubble radius, a reconstruction process has been established in the presence of flow inhomogeneities and for flows with correlated or uncorrelated size-velocity distributions. While spatial gradients of the number density or its flux do not intervene due to symmetry, the spatial curvatures of these quantities have a profound influence on the reconstructed size or joint size-velocity distributions. Orders of magnitude are provided to estimate up to which curvature the classical procedure for homogeneous flow remains valid.

The question of the demodulation of information in the vicinity of walls has also been addressed. A solution has been proposed for the determination of local number density fluxes, and its feasibility has been demonstrated on a particular example. However, starting from the classical raw information available from phase detection probes, no procedure seems available to determine the number density in such two-phase regions.

In practice, since the reconstruction process could produce artifacts, one has to be cautious in the choice of the size resolution. This constraint implies, notably, a very long run of real probe data. Moreover, it could be advantageous to smooth the raw chord or joint chord-velocity distributions issued from phase detection probes, before performing any reconstruction. In the same prospect, these distributions are distorted in the region of the smallest chords, due to the finite size of the probes. To what extent such defects can influence the reconstruction is still an open question.

For all the cases considered, the required sets of hypothesis about the flow structure have been clearly established. The most important limitation of the proposed results is connected with the assumption of a unidirectional flow for the dispersed phase. Improvements can probably be achieved by setting some probability. Alternately, the previous analysis can be extended if two velocity components are measured: a possibility may be the use of two monofiber probes at nearly the same location in connection with the velocity measurement technique based on the transient duration analysis.

References

Achard, J.L., Cartellier, A., 1993. Extra deformation tensor in two-phase flows modeling. In: Proceedings of the fifth International Symposium on Refined Flow Modelling and Turbulence Measurements, Presses de l'E.N. des Ponts et Chaussées, September 7, 10. Paris, France, pp. 477–484.

Cartellier, A., 1992. Simultaneous void fraction measurement, bubble velocity, and size estimate using a single optical probe in gas-liquid two-phase flows. Rev. Sci. Instrum. 63 (11), 5442–5453.

Cartellier, A., 1997. Measurement of gas phase characteristics using new optical probes and real time signal processing. In: Proceedings of the OECD/CNSI Specialist Meeting on Advanced Instrumentation and Measurement Techniques, March 17, 20. Santa Barbara, CA.

Cartellier, A., Achard, J.L., 1991. Review article: local phase detection probes in fluid/fluid two-phase flows. Rev. Sci. Instrum. 62 (2), 279–303.

Cartellier, A., Barrau, E., 1998a. Monofiber optical probes for gas detection and gas velocity measurements: conical probes. Int. J. Multiphase Flow 24 (8), 1265–1294.

Cartellier, A., Barrau, E., 1998b. Monofiber optical probes for gas detection and gas velocity measurements: optimised sensing tips. Int. J. Multiphase Flow 24 (8), 1295–1315.

Cartellier, A., Lismonde, B. 1984. Theoretical model of a grating anemometer for local bubble velocity measurement. Dùrao D, Durst F, eds. Proceedings of the Second International Symposium on Applications of Laser Anemometry to Fluid Mechanics. 18.5.1–6, June 2–4. Lisbon, Portugal.

Cartellier, A., Moechti, Triyogi Y., Achard, J.L., 1993. Plane poiseuille bubbly flows: void fraction and wall shear stress. In: M.D. Kelleher et al. (Ed.). Experimental Heat Transfer, Fluid Mechanics and Thermodynamics, vol. 2. Elsevier, New York, pp. 1402–1409.

Cartellier, A., Barrau, E., Poupot, Ch, Chambérod, E, 1996. Sondes optiques: innovations sur un capteur classique. La Houille Blanche 1 (2), 120–128.

Clark, N., Turton, R., 1988. Chord length distributions related to bubble size distribution in multiphase flows. Int. J. Multiphase Flow 14 (4), 413–424.

Cubizolles, G. 1996. Étude Stéréeologique de la topologie des écoulements diphasiques à haute pression. Doctorat de L'École Centrale de Lyon, Janvier. .

Dubes, R. 1968. The Theory of Applied Probability. Prentice-Hall, New York, EE Series.

Galaup, J-P., 1976. Contribution to the study of methods for measuring two-phase flow, Doctorat. University Scientifique et médicale et INP de Grenoble.

Gouirand, J.M. 1990. Technology and signal treatment development of optical probes for two-phase flow measurements. Proceedings of the Optical Science and Engineering Congress. 12–15 March. The Hague, The Netherlands.

Herringe, R., Davis, M., 1976. Structural development of gas–liquid mixture flows. J. Fluid Mech. 73 (1), 97–123.

Hibiki, T., Hogsett, S., Ishii, M., 1997. Local measurement of interfacial area, interfacial velocity and liquid turbulence in two-phase flow. In: proceedings of the OECD/CSNI Specialist Meeting on Advanced Instrumentation and Measurement Techniques, March 17, 20. Santa Barbara, CA.

Ishii, M., 1975. Thermo-fluid Dynamic Theory of Two-phase Flow. Eyrolles, Paris.

Kataoki, I., Ishii, M., Serizawa, A., 1986. Local formulation and measurements of interfacial area concentration in two-phase flow. Int. J. Multiphase Flow 12 (4), 505–529.

Pinguet, B., 1994. Étude de sondes d'impédance pour la caractérisation d'écoulements diphasiques liquide-liquide en conduite inclinée. Doctoral de l'Univ. Pierre et Marie Curie, Paris.

Revankar, S., Ishii, M., 1993. Theory and measurement of local interfacial area using a four sensor probe in two-phase flow. Int. J. Heat Mass Transfer 36 (12), 2997–3007.

Simonin, O. 1996. Combustion and turbulence in two-phase flows. Lecture Series 1996-02. von Karman Institute for Fluid Dynamics.

Sommerfeld, M., Qiu, H-H., 1995. Particle concentration measurements by phase-doppler anemometry in complex two-phase flows. Experiments in Fluids 18, 187–198.

Zhang, D., Prosperetti, A., 1994. Averaged equations for inviscid disperse two-phase flow. J. Fluid Mech. 267, 185–219.

Zun, I., Filipic, B., Perpar, M., Bombac, A., 1995. Phase discrimination in void fraction measurements via genetic algorithms. Rev. Sci. Instrum. 66 (10), 5055–5064.